Dalton Transactions

ROYAL SOCIETY OF CHEMISTRY

PAPER

View Article Online
View Journal | View Issue

Cite this: *Dalton Trans.*, 2026, **55**, 3840

Magneto-structural correlations in cobalt(II)-phenanthroline compounds with chloranilic acid

Filip Torić, [a] Lidija Androš Dubraja, [a] Mirta Herak, [b] Nikolina Novosel, [b] Irina Petreska, [c] Krešimir Molčanov*[a] and Dijana Žilić *[a]

Received 22nd October 2025,
Accepted 28th January 2026

DOI: 10.1039/d5dt02533h

rsc.li/dalton

The impact of subtle modification of the environment on magnetic properties, by exchanging only solvent molecules, was investigated using a novel series of cobalt(II) compounds as a case study. Three new cobalt(II) complexes with a phenanthroline ligand (phen) and chloranilic acid (CA) [Co(CA)(phen)$_2$] (**1**) were synthesized: **1**·MeOH, **1**·EtOH, and **1**·EtGly. Single-crystal and powder X-ray diffraction revealed that all structures are isostructural mononuclear complexes with a distorted octahedral cobalt environment. X-band ESR spectroscopy provided an effective spin of 1/2 with anisotropic g_{eff}-values for cobalt ions at low temperatures. ESR linewidth analysis, supported by DFT calculations, revealed negligible intermolecular interactions. Static magnetic properties were studied using the temperature and field dependence of magnetization. Comprehensive magnetic modeling of the experimental data provides deeper insight into the subtle influence of different crystal packing arising from solvent exchange on the magnetic properties of the complexes. Additionally, AC magnetic susceptibility studies at low temperatures revealed field-induced slow magnetization relaxation in these cobalt(II) compounds.

1. Introduction

Chloranilic acid (2,5-dichloro-3,6-dihydroxy-1,4-benzoquinone, CA) is a highly versatile ligand capable of coordinating to transition metals in a variety of coordination modes, the most common ones being bridging (bis)bidentate and terminal bidentate.[1] Its uniquely malleable π-electronic structure is sensitive to (de)protonation states and coordination modes; while in bridging (bis)bidentate mode it has two delocalised systems separated by single C–C bonds, its terminal bidentate mode has an *o*-quinoid structure.[2] It is widely used in coordination chemistry and design of metal–organic frameworks[3–6] with a wide variety of topologies.[6–11] In addition to serving as an excellent bridging ligand, chloranilic acid has several potential sites for hydrogen bonding, charge transfer, and other interactions, making it useful for forming various supramolecular complexes.

Mononuclear cobalt(II) complexes stand out from the transition metal family due to their complicated magnetic description because of significant spin–orbit coupling.[12] In tetrahedral cobalt(II) compounds, the orbital angular momentum is quenched, and therefore it is justified to use the spin Hamiltonian approach. The true *g*-values correspond to the *g*-values in the original $S = 3/2$ spin Hamiltonian, which are approximately 2.0.[13] In octahedral Co(II) compounds, the ground orbital state is t_{2g}, and the degeneracy of the $d_{x^2-y^2}$ and d_{xy} orbitals is removed, so their contribution to orbital angular momentum is quenched. However, the contribution from the degeneracy of d_{xz} and d_{yz} can still remain, and the total orbital angular momentum could be non-quenched. In cases where a large portion of orbital angular momentum remains, the simple spin Hamiltonian approach is not valid anymore, and the relationship between the effective *g*-values and other parameters becomes complicated.[13–15] Therefore, tailoring the ligand field around the cobalt center plays a crucial role in manipulating the magnetic and electronic properties of the targeted compound.[16,17] Besides significant ligand influence, intermolecular interactions can also play a crucial role, which in turn changes the magnetic properties of the material.[18–20] However, it has also been known that small variations beyond the first coordination sphere can also influence the zero-field splitting parameters of the cobalt ion.[12] These factors can complicate the synthesis of complexes with desired magnetic anisotropy parameters and they should be further investigated.

In this work, we present single-crystal and powder X-ray diffraction, elemental analysis, electron spin resonance (ESR) and magnetization studies of novel Co(II)-chloranilate complexes [Co(CA)(phen)$_2$] (**1**; phen = 1,10-phenanthroline) with three solvents: methanol (MeOH), ethanol (EtOH), and ethyl-

[a]*Ruđer Bošković Institute, Bijenička cesta 54, 10000 Zagreb, Croatia. E-mail: kresimir.molcanov@irb.hr, dijana.zilic@irb.hr*
[b]*Institute of Physics, Department for Research of Materials under Extreme Conditions, Bijenička cesta 46, 10000 Zagreb, Croatia*
[c]*Ss. Cyril and Methodius University in Skopje, Faculty of Natural Sciences and Mathematics – Skopje, Institute of Physics, PO Box 162 1000 Skopje, Macedonia*

ene glycol (EtGly). Despite their very similar molecular structures, the local and bulk magnetic structures of the **1**·solvent complexes reveal small but noticeable differences. Computational methods and DFT calculations, in tandem with experimental ESR and SQUID results, were used to interpret the magnetic behavior and establish magneto-structural correlations in the investigated cobalt(II) complex solvates. To probe the potential of these complexes for single-molecule magnet properties, AC magnetic susceptibility was measured both in the absence and in the presence of a magnetic field.[12,17]

2. Results

2.1. Crystal structures

The following solvates of compound **1** were prepared: **1**·MeOH, **1**·EtOH, and **1**·EtGly. They are isostructural and comprise a C_2-symmetric molecule of **1** (with the Co atom located on a twofold axis, which also passes through the chloranilate moiety, Fig. 1) and a solvent molecule located on a twofold axis. Compound **1** (Fig. 1) is analogous to previously published Cu(II)-CA and Ni(II)-CA complexes with ancillary ligands 2,2′-bpy[21] and 1,10-phen;[22,23] they comprise a single CA dianion (bound as a terminal bidentate ligand) and two bpy or phen molecules bound to the metal centre. The uniformity and crystallinity of the bulk products were confirmed by powder X-ray diffraction (PXRD) and elemental analysis. The PXRD patterns shown in Fig. S7 in the SI of compounds **1**·MeOH, **1**·EtOH, and **1**·EtGly correspond closely to those simulated from the single-crystal data of these compounds at room temperature, indicating that structural integrity is maintained in the bulk materials subsequently used for magnetic measurements.

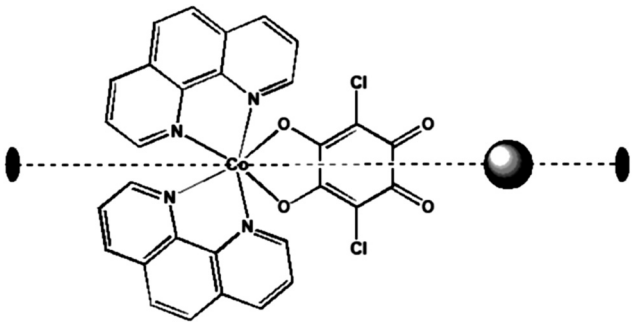

Fig. 1 A molecule of **1** with a twofold symmetry axis marked as a dashed line. The position of the solvent molecule is indicated by a grey sphere.

In compound **1**, the Co(II) ion is hexacoordinated in a distorted octahedral environment (Table 1). The calculations of the continuous shape measures (Table 2) show no significant differences in the coordination sphere of cobalt(II) across all complexes,[24] as can be seen from the overlaid structures in Fig. 2. Even more detailed measures for octahedral distortion that are commonly used, ζ, Δ and Σ (ref. 25) (see the SI for expressions), are similar across all complexes. The chloranilate ligand coordinates the metal as a terminal bidentate ligand[21,22] and has an *o*-quinoid structure[21–23] (Table S3). The coordination sphere is completed by two phenanthroline ligands. A solvent molecule is hydrogen-bonded to the chloranilate moiety and occupies a cavity located on the twofold axis (Fig. 1 and Fig. 3). Since both molecule **1** and the solvent are located on the twofold axis, the asymmetric unit contains a half of each.

The studied compounds differ in the steric size, symmetry, polarity and proton donating capabilities of the solvent

Table 1 Geometric parameters of cobalt(II) coordination spheres (Å, °)

	1·EtGly@100K	**1**·EtGly@RT	**1**·MeOH@100K	**1**·MeOH@RT		**1**·EtOH@100K	**1**·EtOH@RT
Co1–O1	2.081(3)	2.0844(18)	2.0843(14)	2.0836(11)	Co1–O1	2.0863(12)	2.0857(16)
Co1–N2	2.111(3)	2.115(2)	2.1217(17)	2.1262(15)	Co1–O2	2.0847(11)	2.116(2)
Co1–N1	2.133(3)	2.135(2)	2.1265(16)	2.1280(13)	Co1–N1	2.1095(15)	2.1342(19)
O1–Co1–N1	93.68(12)	167.57(7)	92.50(6)	90.86(5)	Co1–N2	2.1309(14)	94.42(7)
O1–Co1–N2	92.48(12)	91.81(8)	94.02(6)	166.66(5)	Co1–N3	2.1343(13)	92.82(7)
O1–Co1–O1^{i}	78.73(11)	78.32(7)	78.67(5)	78.44(5)	Co1–N4	2.1137(15)	78.33(6)
O1–Co1–N1^{i}	167.24(12)	94.42(7)	90.27(6)	92.74(5)	O1–Co1–O2	78.63(5)	167.64(6)
O1–Co1–N2^{i}	91.39(12)	92.87(8)	166.51(5)	94.31(5)	O1–Co1–N1	91.25(5)	91.82(7)
N1–Co1–N2	78.60(13)	78.38(9)	78.65(6)	78.20(5)	O1–Co1–N2	166.70(5)	78.42(8)
N1–Co1–O1^{i}	167.24(12)	94.42(7)	90.27(6)	92.74(5)	O1–Co1–N3	93.38(5)	167.64(6)
N1–Co1–N1^{i}	95.51(12)	94.41(8)	176.42(6)	175.35(5)	O1–Co1–N4	92.19(5)	94.37(7)
N1–Co1–N2^{i}	97.99(13)	97.46(9)	98.91(6)	98.60(5)	O2–Co1–N1	92.49(5)	97.45(8)
N2–Co1–O1^{i}	91.39(12)	92.87(8)	166.51(5)	94.31(5)	O2–Co1–N2	92.93(5)	91.82(7)
N2–Co1–N1^{i}	97.99(13)	97.46(9)	98.91(6)	98.60(5)	O2–Co1–N3	167.30(5)	97.45(8)
N2–Co1–N2^{i}	175.00(12)	173.97(8)	98.91(6)	94.87(5)	O2–Co1–N4	91.79(5)	174.01(7)
O1^{i}–Co1–N1^{i}	93.68(12)	167.57(7)	92.50(6)	90.86(5)	N1–Co1–N2	78.75(6)	94.42(7)
O1^{i}–Co1–N2^{i}	92.48(12)	91.81(8)	94.02(6)	166.66(5)	N1–Co1–N3	97.57(5)	92.82(7)
N1^{i}–Co1–N2^{i}	78.60(13)	78.38(9)	78.65(6)	78.20(5)	N1–Co1–N4	174.97(5)	78.42(8)
					N2–Co1–N3	96.60(5)	
					N2–Co1–N4	98.38(6)	
					N3–Co1–N4	78.56(5)	

Symmetry operator: ^{i} $1-x, y, 3/2-z$.

Table 2 Continuous shape measures (CShM), ζ, Δ and Σ, as defined in the SI, for the CoN_4O_2 octahedron in the studied complexes, calculated using the OctaDist repository[25]

Complex	T/K	CShM	Z	Δ	Σ
1·EtGly	100	1.1611	0.1087	0.000107	70.6686
1·EtGly	RT	1.1784	0.1083	0.000098	72.4468
1·EtOH	100	1.1717	0.09839	0.000084	70.6442
1·EtOH	RT	1.1684	0.1054	0.000089	72.2221
1·MeOH	100	1.2130	0.1061	0.000079	70.6781
1·MeOH	RT	1.2516	0.1161	0.000094	73.0507

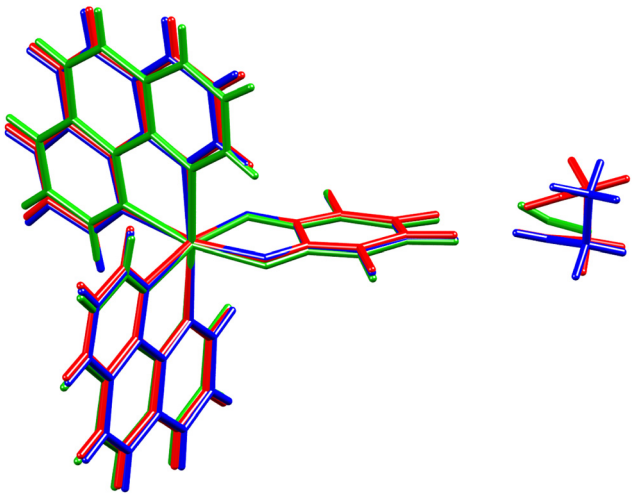

Fig. 2 Overlaid structures of **1**·MeOH (green), **1**·EtOH (blue), and **1**·EtGly (red) recorded at 100 K.

molecules. EtOH and MeOH have a C_1 symmetry and are single-proton donors, while EtGly is a C_2-symmetric double proton donor. Therefore, EtOH and MeOH located in a special position with C_2 symmetry are disordered over two positions, while EtGly is ordered at 100 K, but at room temperature displays dynamic disorder. In addition, the double proton donor EtGly is capable of forming two symmetry-equivalent hydrogen bonds to the chloranilate moiety (with atom O1 as an acceptor, Fig. 4), while EtOH and MeOH form only one (Table 3).

An interesting aspect of these structures is the ordering of the solvent at 100 K and disorder at room temperature. The ethanol molecule in **1**·EtOH at RT is disordered about the twofold axis (Fig. 4a), but at 100 K, it is ordered. Ordering of the ethanol molecule in **1**·EtOH at 100 K leads to a phase transformation: the RT $C2/c$ unit cell transforms to $P2_1/n$. Due to the lower symmetry at 100 K, both the molecule of **1** and ethanol are located in a general position; therefore, the asymmetric unit contains a single molecule of **1** and a single, ordered molecule of ethanol (Fig. 4b). The overall crystal packing in both cells remains unchanged, so the $P2_1/n$ cell has pseudo-systematic absences consistent with C-centering. However, the structure solution in the space group $C2/c$ yielded a disordered structure. The situation in **1**·EtGly is similar, with the solvent at 100 K being ordered, forming two hydrogen bonds to the chloranilate moiety (Fig. 4c), but at room temperature its conformation changes due to a dynamic disorder. However, there is no phase transformation in **1**·EtGly. In **1**·MeOH, the solvent is disordered about the twofold axis at both temperatures. In addition to hydrogen bonds, all complexes exhibit similar aromatic stacking interactions. Details of aromatic stacking geometry can be found in Table S4 in the SI.

2.2. ESR study

The complexes were investigated by electron spin resonance (ESR) or electron paramagnetic resonance (EPR) spectroscopy. At room temperature, the complexes were ESR silent due to the fast spin–lattice relaxation.[26] Representative spectra, obtained at three selected low temperatures, are shown in Fig. 5. The spectra are highly anisotropic with three or four distinct features. The direct comparison of the spectra of different solvates, presented as ESR intensity *vs.* g-values to avoid B-shift due to slightly different microwave frequencies, can be seen in Fig. 5(b).

The simulation of the spectra was performed with EasySpin software[27] using the reduced form of the spin Hamiltonian for Co(II) ions:[28]

$$H = \mu_B \cdot B \cdot g \cdot S \quad (1)$$

where B is the magnetic field, g is the g-tensor, and the constant μ_B is the Bohr magneton. For octahedral Co(II) ions in the high-spin state, spin $S = 3/2$ couples to the orbital angular momentum L with the strength λ of spin–orbit coupling.[26] In the ground state, only the lowest levels are thermally occupied as can be seen later in Fig. 11. As a result, effective spin $S_{eff} = 1/2$ can be used to describe the observed ESR line with very anisotropic g-values.[26,28–31] A hyperfine interaction for Co(II) ions was not detected and therefore this term is omitted from eqn (1). Consequently, the spectra were simulated using an anisotropic g-tensor with an assumed Gaussian line shape. g-Strain parameters were also included in the simulation to account for the small distribution of g principal values.[32] The principal g-values obtained at different temperatures are presented in Table 4, along with the average g-values at 5 K. The fact that it was not possible to simulate the spectra at different temperatures using the same g-values suggests a different population of spin states at varying temperatures. The obtained anisotropic g-values are in agreement with the distorted octahedral structure around Co(II) ions and with the values for similar Co(II) geometry reported in the literature.[30,33–35]

The nearest cobalt–cobalt distances, according to the structure recorded at 100 K, are around 8.5 Å: 8.44, 8.57 and 8.54 Å for **1**·MeOH, **1**·EtOH and **1**·EtGly, respectively. To estimate intermolecular coupling, we calculated the dipolar contribution to the ESR linewidth. Using the method of moments,[36,37] the linewidths due to dipolar interactions of cobalt spin $S_{eff} = 1/2$ with spins of all cobalt ions in the sphere of radius 15 Å are $\Gamma_d \approx 27$–28 mT (Table 4). The positions of cobalt spins are taken from the crystallographic data obtained

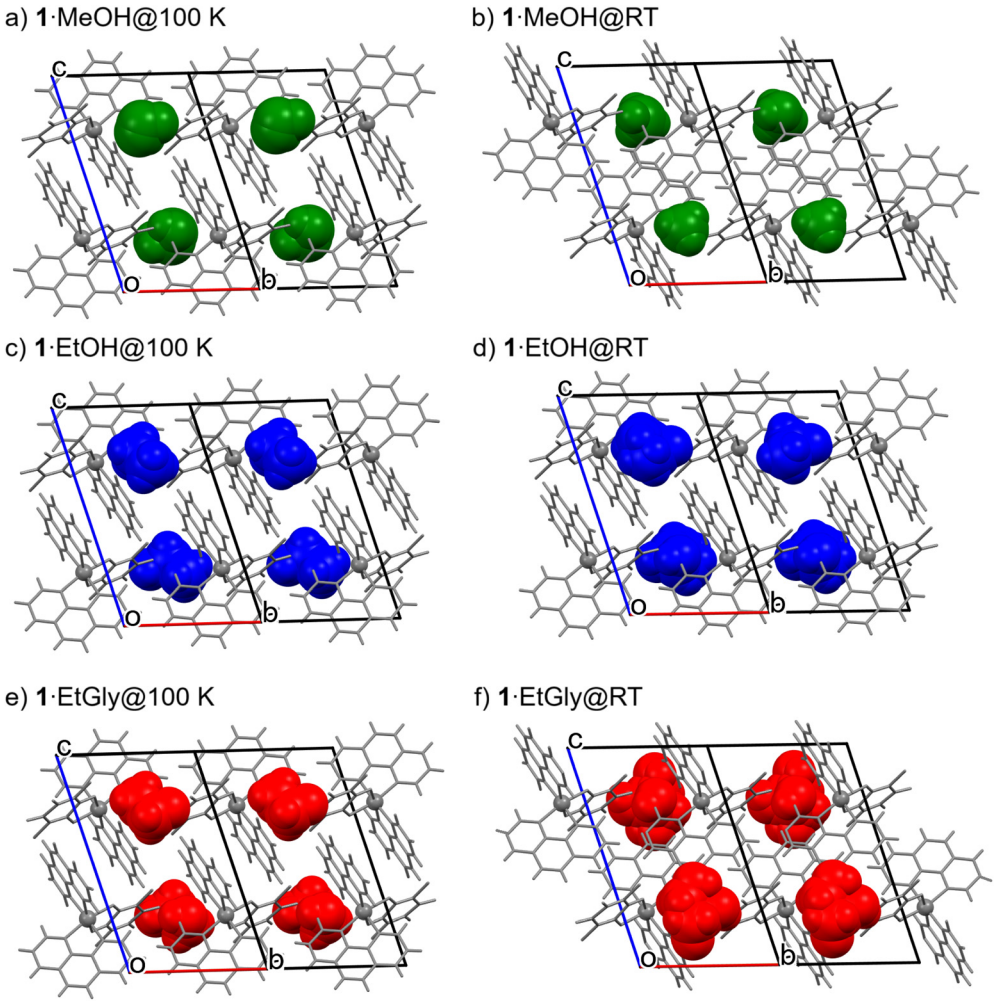

Fig. 3 Crystal packing of **1**·MeOH (a, b), **1**·EtOH (c, d) and **1**·EtGly (e, f) recorded at 100 K and room temperature (RT) viewed in the [–1 1 0] direction. Molecules of **1** are grey, and solvent molecules are shown in green (MeOH), blue (EtOH), and red (EtGly) in the space-fill representation.

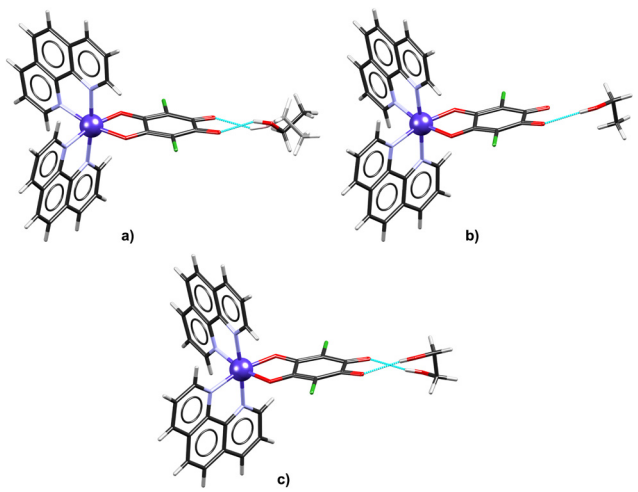

Fig. 4 Hydrogen-bonded motif of crystal packing in (a) **1**·EtOH at RT with a disordered ethanol molecule (the other component of the disorder is drawn in a pale colour), (b) **1**·EtOH at 100 K with an ordered molecule of ethanol and (c) **1**·EtGly at 100 K with an ordered molecule of ethylene glycol.

Table 3 Geometric parameters of hydrogen bonds

Complex	D–H/Å	H···A/Å	D···A/Å	D–H···A/°	Symm. op. on A
1·EtGly@100 K					
O3–H3···O2	0.84	2.06	2.795(9)	146	*x*, *y*, *z*
1·EtGly@RT					
O3–H3···O2	0.83	2.17	2.275(2)	124	*x*, *y*, *z*
1·EtOH@100 K					
O5–H5···O4	0.84	2.02	2.7947(18)	153	*x*, *y*, *z*
1·EtOH@RT					
O3–H3···O2	0.82	2.00	2.699(8)	142	*x*, *y*, *z*
1·MeOH@100 K					
O3–H3···O2	0.84	2.15	2.770(3)	130	*x*, *y*, *z*
1·MeOH@RT					
O3–H3···O2	0.82	2.11	2.773(5)	138	*x*, *y*, *z*

at 100 K. Experimentally observed linewidths, taken from ESR simulations at 5 K, are around 25 mT (Table 4). Applying the linewidth analyses:[38,39]

$$\Gamma_{\mathrm{exp}} \approx \gamma {\Gamma_{\mathrm{d}}}^2 / \sqrt{J[S(S+1)]}, \quad (2)$$

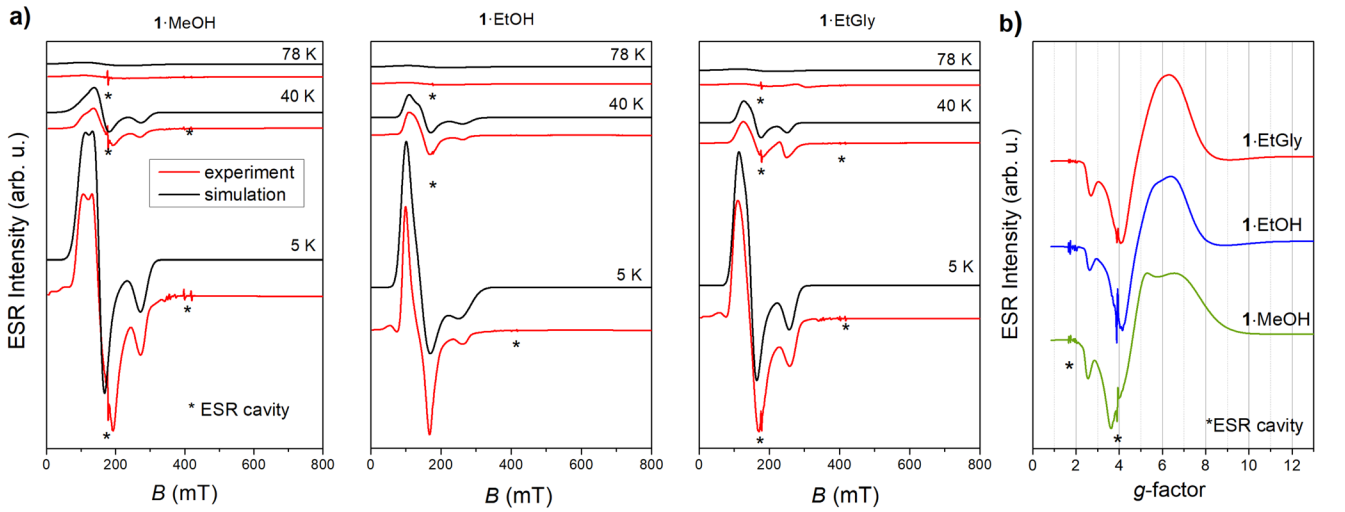

Fig. 5 (a) Experimental (red lines) and simulated (black lines) ESR spectra of polycrystalline samples of the investigated complexes. The ESR intensities of the spectra at different temperatures are presented in the real ratios. The weak, narrow lines labeled with asterisks originate from the ESR cavity. (b) Comparison of the experimental ESR spectra presented as ESR intensity *vs.* *g*-factor of the investigated complexes recorded at the lowest measured temperature of 5 K.

where γ is the gyromagnetic ratio, the intermolecular-coupling constant was estimated to have a value of $J \approx 0.07$–0.09 cm^{-1}, given in Table 4. The presence of weak intermolecular coupling is consistent with the Gaussian line shape assumed in the simulation of the ESR spectra, in contrast to the Lorentzian shape observed for strongly coupled spins.[37]

2.3. Magnetization study

Field dependence. Fig. 6 shows the magnetic field dependence of the induced magnetic moment measured at $T = 1.8$ K for the three complexes **1**·MeOH, **1**·EtOH and **1**·EtGly. Magnetic hysteresis was not detected for any of the samples. In addition to experimental data, the Brillouin functions at the lowest measured temperature, $T = 1.8$ K, assuming a spin state $S = 1/2$ and an average *g*-value g_{av} from ESR simulations at 5 K (Table 4), are also shown. None of the complexes exhibits behaviour described by the Brillouin function, which includes a spin-only contribution and describes the non-interacting spin $S = 1/2$. However, in a high field around 7 T, the magnetic moment saturates. The saturated moment obtained for **1**·MeOH agrees well with the saturated moment obtained from the Brillouin function $\mu_{sat} = S \cdot g_{av} = 1/2 \cdot g_{av}$. For two other complexes, **1**·EtGly and **1**·EtOH, we obtain effective moments slightly smaller than expected for spin-only $S = 1/2$ and g_{av} of a noninteracting system.[26,31]

Temperature dependence. In Fig. 7, we plot the temperature dependence of the product of molar susceptibility and temperature, χT. The values of magnetic moment μ_{eff} at high temperatures saturate to magnitudes that are in agreement with high-spin $S = 3/2$ for Co^{2+} in an octahedral environment, where incomplete quenching of orbital angular moment leads to an increased moment magnitude in comparison with the spin-only value of $3.87\mu_B$/Co.[40–42] The moment values at 300 K reach $5.1\mu_B$/Co for all three complexes, **1**·MeOH, **1**·EtGly, and **1**·EtOH (Fig. S8), comparable to values found for the Co^{2+} ion in an octahedral environment in some complexes.[40–42] As the temperature decreases, μ_{eff} decreases in all complexes. The decrease of μ_{eff} at low temperatures in cobalt octahedral compounds in a N_4O_2 environment found in the literature[16,41,43–52] is associated with the spin–orbit coupling, which results in an $S_{eff} = 1/2$ ground state and lowering of the population of higher excited state as the temperature decreases. The presence of spin–orbit coupling makes the magnetic analysis of cobalt compounds not straightforward.

Table 4 The principal *g*-values [g_x g_y g_z] obtained from the simulations of ESR spectra using spin Hamiltonian (1) and assuming effective spin $S_{eff} = 1/2$

Complex	**1**·MeOH	**1**·EtOH	**1**·EtGly
		***g*-Values**	
78 K	[2.54 4.5 6.7]	[2.6 4.5 6.45]	[2.75 5.0 5.1]
40 K	[2.53 4.4 6.0]	[2.6 4.5 6.45]	[2.75 4.3 5.6]
5 K	[2.54 4.57 6.6]	[2.65 4.7 6.9]	[2.68 4.65 6.3]
5 K	$g_{av} = 4.86$	$g_{av} = 5.06$	$g_{av} = 4.78$
		Linewidths	
Γ_{exp} (mT)	24	25	25
Γ_d (mT)	27.9	28.2	26.7
J (cm^{-1})	0.08	0.09	0.07

The average *g*-value is calculated as $g_{av} = \sqrt{(g_x^2 + g_y^2 + g_z^2)/3}$. Experimental Γ_{exp} and dipolar Γ_d linewidths, defined in the text, and the calculated intermolecular coupling constant J are given.

2.4. Magnetic modeling

As the octahedral environment of the investigated Co(II) ions is highly distorted and far from O_h crystal symmetry, magnetic

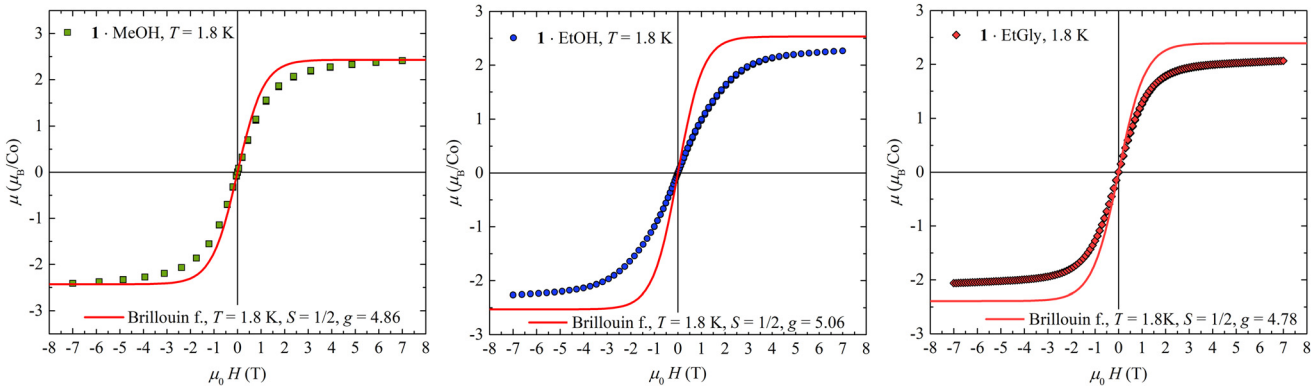

Fig. 6 Magnetic field dependence of the induced magnetic moment in the three complexes, **1**·MeOH, **1**·EtOH, and **1**·EtGly, measured at T = 1.8 K. The red solid line represents the Brillouin function at T = 1.8 K for S = 1/2 with g_{av} from the ESR simulation given in Table 4.

data were first reproduced using a simple spin Hamiltonian for spin S = 3/2 with axial and rhombic anisotropy, which is commonly used when analysing Co(II) magnetic data:

$$H = \mu_B g \mathbf{S} \cdot \mathbf{B} + D\left(S_z^2 - \frac{S(S+1)}{3}\right) + E(S_x^2 - S_y^2) \qquad (3)$$

where D and E are the axial and rhombic zero-field splitting parameters, respectively. The obtained best-fit parameters are given in Table 5. The fitted curves plotted in Fig. 7 correspond to χ_{TOT}

$$\chi_{TOT}(T) = \chi_{Ham}(T) + \chi_{dia} + \chi_{TIP} \qquad (4)$$

where χ_{Ham} is the result obtained by the procedure described above based on Hamiltonian (3), χ_{dia} includes the temperature-independent diamagnetic contribution of the samples, as well as the sample holder, and χ_{TIP} is the temperature-independent paramagnetism, also given in Table 5. The values for axial D and rhombic E magnetic parameters were given as absolute values, as it is not possible to distinguish the sign.

Besides the use of simple spin Hamiltonian (3), we have extended our research by reproducing the measured magnetic susceptibility data using the Hamiltonian that contains orbital and spin Zeeman terms, spin–orbit coupling, and local environment anisotropies. Here, we used a simplified model, in which orbital spin L = 3 is reduced to $\tilde{L}$ = 1 using an isomorphism between the orbital triplet $^4T_1$ coming from the ^4F term and triplet $\tilde{L}$ = 1 from ^4P.[28] Furthermore, a distorted octahedral environment, which is reflected in anisotropic g-values obtained from the ESR study, suggests a need to use both axial and rhombic anisotropies to reproduce the susceptibility data:[28]

$$H = \mu_B g_e \mathbf{S} \cdot \mathbf{B} - \frac{3}{2}\mu_B \kappa \mathbf{L} \cdot \mathbf{B} - \frac{3}{2}\kappa\lambda \mathbf{L} \cdot \mathbf{S} + \Delta_{ax}\left(L_z^2 - \frac{2}{3}\right) + \Delta_{rh}(L_x^2 - L_y^2) \qquad (5)$$

where λ is the spin–orbit coupling parameter for Co(II) ions, κ is the orbital reduction factor, and Δ_{ax} and Δ_{rh} are axial and rhombic distortion parameters. In general, reproducing measured data using Hamiltonian (5) and obtaining reliable fit parameters for Co(II) octahedral complexes have proven very challenging. Interestingly, using Cambridge Crystallographic Data Centre (CCDC) ConQuest Software[53] query for N_4O_2 Co(II) octahedra, we were able to identify only 12 articles where magnetic data were reproduced using a Hamiltonian containing spin–orbit coupling parameters,[16,41,43–52] with different fit qualities ranging from good to poor. A promising direction for improving the reliability of Co(II) magnetic parameters and preventing over- and under-parametrization is a joint modeling approach that combines ESR results with static magnetization data.[52] In our research, Hamiltonian (5) is diagonalized and fitted using our own developed code written in *Python*, which enabled us to perform (1) a grid search with fixed parameters, such as the κ parameter, (2) explore over a variety of initial guesses, and (3) include ESR data information into the fitting procedure. As the measurements were performed on the powder sample, the corresponding magnetization from Hamiltonian (5) was calculated for powder approximation, with details in section S2.5 in the SI. As Δ_{ax} and Δ_{rh} are particularly sensitive to over-parametrization, using the joint modeling enabled fitting only one of them, Δ_{ax}, and the other one is then calculated as the closest value that would correspond to the ESR-obtained g-values by combining the energy levels of two Hamiltonians, (1) and (5). This enabled us to obtain as reliable magnetic parameters as possible for **1**·MeOH, **1**·EtGly and **1**·EtOH complexes, which are summarized in Table 6, while the best-fitted curves are shown in Fig. 7. As can be seen, the fitted curves from both Hamiltonians (3) and (5) are similar, pointing to the small orbital contribution in these cobalt(II) compounds.

The obtained spin–orbit coupling parameter λ of −118, −117 and −128 cm^{-1} for **1**·MeOH, **1**·EtOH and **1**·EtGly, respectively, are in good agreement with the reported values for the Co(II) complexes with N_4O_2 crystal surroundings ranging between −108 and −180 cm^{-1}.[16,41,43–51] We obtained a negative axial distortion parameter Δ_{ax} for all complexes, which suggests axial elongation along the z magnetic axis. The crystallographic axes are not unambiguously related to the mag-

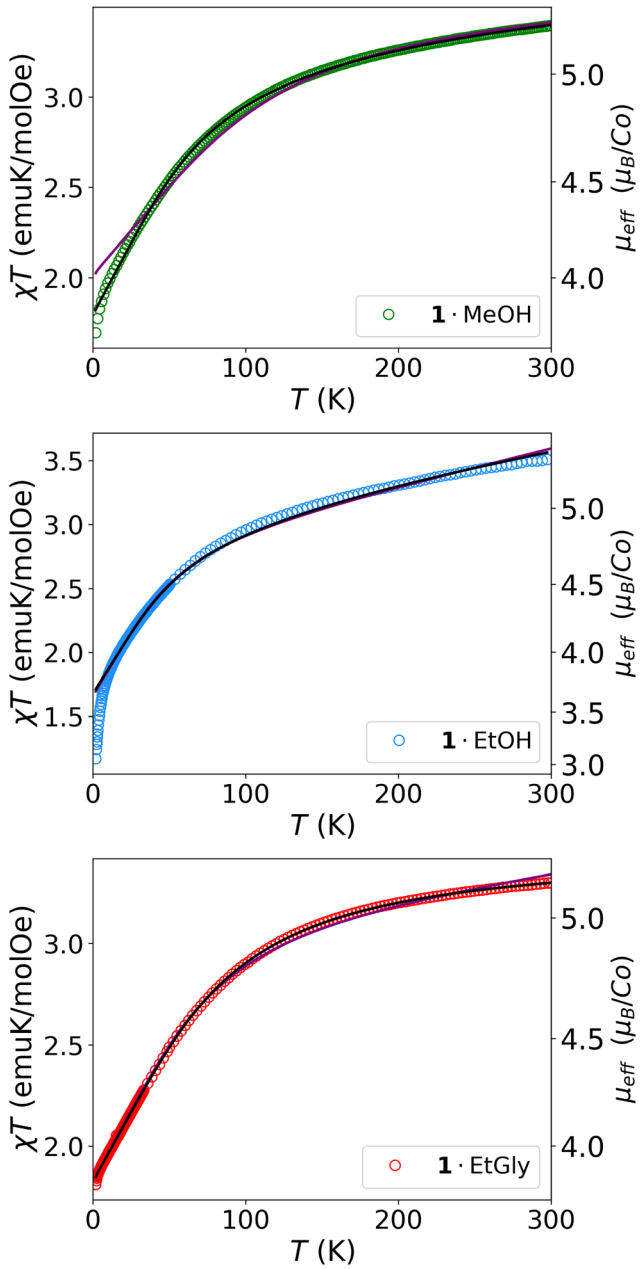

Fig. 7 Temperature dependence of the product of molar susceptibility and temperature χT for the **1**·MeOH, **1**·EtOH and **1**·EtGly complexes, measured in an applied magnetic field of $\mu_0 H$ = 0.1 T. Axes on the right show the corresponding effective magnetic moment obtained from the expression $\sqrt{8\chi T}$. The purple and black solid lines represent the best-fitted model curve to Hamiltonians (3) and (5), respectively, given by expression (4).

Table 5 Summarized best-fit parameters of magnetic susceptibility based on spin Hamiltonian model (3)

Complex	g	$\lvert D\rvert$ [cm^{-1}]	E [cm^{-1}]	TIP [emu mol^{-1}]	R^2
1·MeOH	2.55	59.97	6.43	0.0014	0.9980
1·EtOH	2.42	40.12	11.72	0.0028	0.9781
1·EtGly	2.53	63.62	8.41	0.0012	0.9990

R^2 is a goodness-of-fit measure.

netic axis of Hamiltonian (5), but we can assume that the z-magnetic axis is oriented along the crystallographic twofold symmetry axis given in Fig. 1. Reported Δ_{ax} values in the literature span across a wide range from −1803 cm^{-1} to 892 cm^{-1}.[16,43–52] Using these values, a plot of the maximum divergence from the planarity of *trans* angles in Co octahedral (Δ_{planar}), calculated using eqn (6) and the Δ_{ax} values, is shown in Fig. 8.

$$\Delta_{planar} = \max_{trans\ angle\ \theta} (180° - \theta) \quad (6)$$

For this analysis, we have taken only complexes for which oxygens in the Co octahedral are in the *cis* position, as is the case in the investigated complexes. It is interesting to see that by examining this simple structural feature, Δ_{ax} values of N_4O_2 Co(II) octahedra seem to follow a line. The only value that differs from this line is the value for $C_{29}H_{42}Br_2Co_3N_{14}O_8$ from ref. 47. Besides the magnetic parameters from Hamiltonian (5), Mocanu *et al.* modeled exchange interactions between Co magnetic centers and this could be the reason for this discrepancy due to potential fit overestimation. This line dependence would imply the existence of a Δ_{planar} value for which the magnetic axial distortion diminishes. There is no particular physical basis for this, and therefore this correlation near zero should be treated with caution. Nevertheless, for larger divergences from the planarity of Co octahedral *trans* angles, larger positive magnetic axial distortions could be expected, while the negative magnetic axial distortions can be expected for smaller divergences from planarity.

Furthermore, the energy levels for **1**·MeOH are shown in Fig. 11 and those for **1**·EtOH and **1**·EtGly are shown in Fig. S9 and S10 in the SI. From the energy diagrams, it is clear that only the lowest doublet J = 1/2 is populated at the low temperature as the energy gap separating J = 1/2 and J = 3/2 is 197 cm^{-1}, 151 cm^{-1} and 231 cm^{-1}, for **1**·MeOH, **1**·EtOH and **1**·EtGly, respectively.

2.5. AC magnetic susceptibility study

Magnetization relaxation was investigated using AC (alternating current) susceptibility measurement, both in the absence of the applied static magnetic field and under an applied static field of 1000 Oe. Fig. S11 shows the frequency dependence of the in-phase (χ^{Prime}) and out-of-phase (χ'') components of magnetic susceptibility measured in zero applied static field with the compensation of Earth's magnetic field at the lowest experimentally attainable temperature (1.3 K). It can be readily seen that all samples display fast relaxation of magnetization in the frequency range 1–1000 Hz, *i.e.*, χ^{Prime} is frequency independent and χ'' is practically zero (at least two orders of magnitude smaller than χ^{Prime}). The situation drastically changes upon applying a static magnetic field. Frequency dependence of χ^{Prime} and χ'' measured at several low temperatures in the applied static magnetic field (1000 Oe) for samples **1**·MeOH, **1**·EtOH and **1**·EtGly is shown in Fig. 9. Non-zero values of χ'', as well as a clear frequency dependence of both χ' and χ'' AC susceptibility components, are hallmarks of slow relaxation processes in these systems. Such behaviour resembles the

Table 6 Summarized best-fit parameters of magnetic susceptibility based on spin Hamiltonian model (5)

Complex	κ	λ [cm^{-1}]	Δ_{ax} [cm^{-1}]	$\lvert\Delta_{rh}\rvert$ [cm^{-1}]	TIP [emu mol^{-1}]	R^2
1·MeOH	0.94	−118	−435	155	0.0012	0.9990
1·EtOH	0.78	−117	−421	141	0.0027	0.9759
1·EtGly	0.85	−128	−462	83	0.0010	0.9999

R^2 is a goodness-of-fit measure.

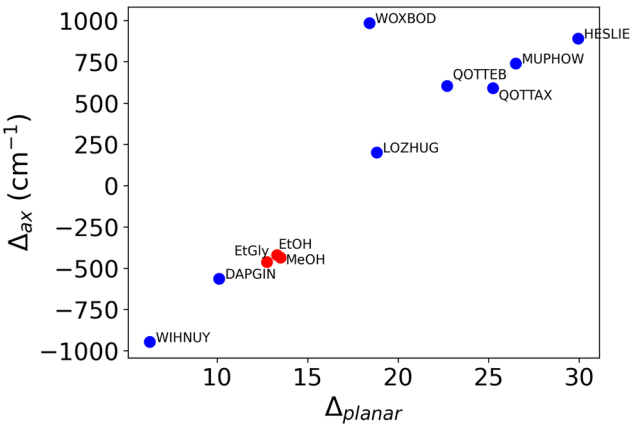

Fig. 8 Correlation between the maximum divergence from the planarity of *trans* angles in Co octahedra and the value of magnetic axial distortion. Besides complexes from this work, on the top of each data point label corresponds to the name of the complex from the CCDC base.

field-induced superparamagnetic slow relaxation of magnetization observed in single-molecular magnets, which has been previously reported in similar compounds.[12,54,55]

Slow relaxation for **1**·EtOH and **1**·EtGly compounds in a magnetic field is analysed within the Debye model,[56] assuming a single relaxation time, which is justified considering that the intermolecular interactions in these systems are negligible. For each temperature, the characteristic relaxation time τ was determined from the peak in $\chi''(f)$ curves (Fig. 10). The experimental data of the spin–lattice relaxation rate (τ^{-1}) are fitted to the combination of one-phonon direct and two-phonon Raman processes:[17]

$$\tau^{-1} = A_{\mathrm{dir}}T + R_{\mathrm{Raman}}T^9. \quad (7)$$

The Orbach process is neglected here, as it involves a "real" transition to the intermediate energy level.[17] The obtained fitting curves are presented in Fig. 10 and the corresponding values of fitting parameters are A_{dir} = (205 ± 8) and (940 ± 60) s^{-1} K^{-1}; B_{Raman} = (0.019 ± 0.002) and (0.08 ± 0.02) s^{-1} K^{-9} for **1**·EtOH and **1**·EtGly, respectively.

Field-induced slow relaxation of magnetization in cobalt compounds could be related to time-reversal symmetry that prevents some spin–phonon processes in the applied magnetic field.[17] Hyperfine interaction can open relaxation paths at zero magnetic field, and slow relaxation is observed only under an external field.[17] Also, the absence of slow relaxation in zero applied static field could be associated with quantum tunnelling of magnetization between degenerate energy levels, a process that is much faster than the time scale of the AC susceptibility experiment. Detailed analysis of the origin of slow magnetic relaxation in these compounds is left for future work.

2.6. DFT study

To further elucidate the observed magnetic behavior of the studied complexes, we carried out single-point DFT (density

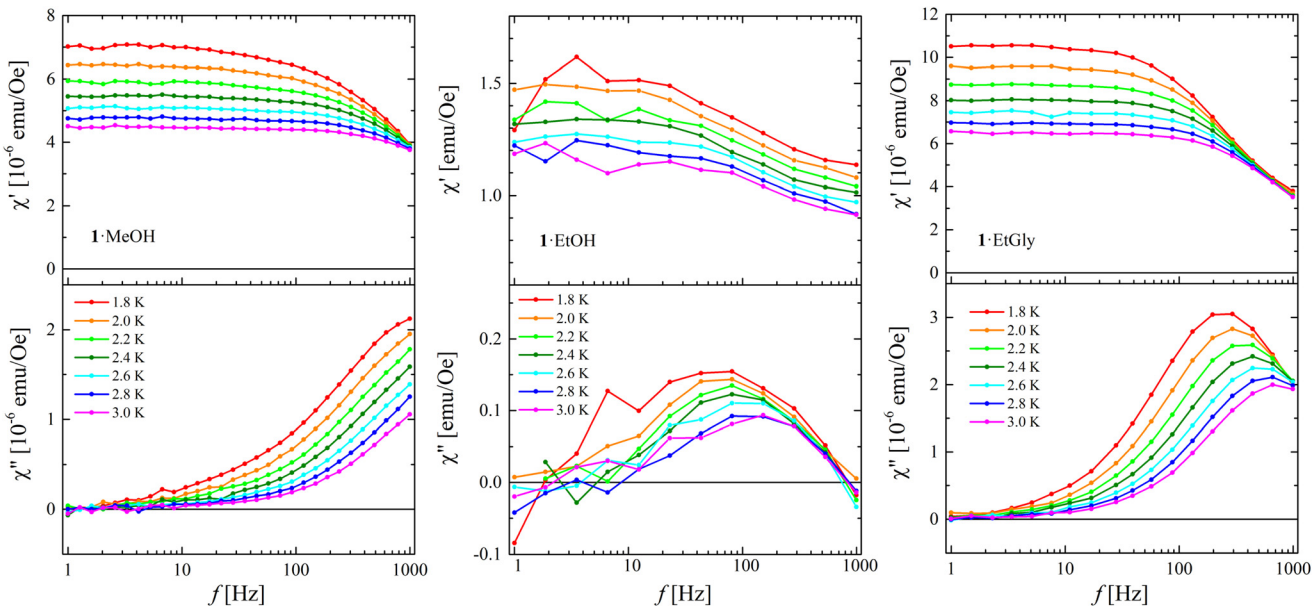

Fig. 9 In-phase χ' and out-of-phase χ'' components of AC magnetic susceptibility measured at various temperatures in the range of 1.8–3.0 K in an applied external static magnetic field of 1000 Oe for the **1**·MeOH, **1**·EtOH and **1**·EtGly compounds.

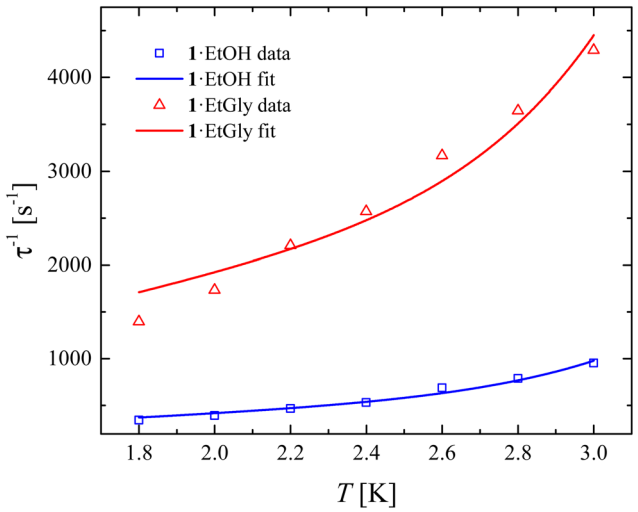

Fig. 10 Temperature dependences of the relaxation rates for the **1**·EtOH and **1**·EtGly compounds. The solid lines are fits based on eqn (7) with parameters given in the text.

functional theory) calculations at the B3LYP/LANL2DZ level of theory.[57,58] The geometry of the unit cell from the recorded structures at 100 K was used in our calculations. We have performed DFT calculations on the doublet, *i.e.*, the low-spin (LS, $S = 1/2$) state, and the quartet, *i.e.*, the high-spin (HS, $S = 3/2$) state. The results confirmed that the HS state is the ground state in all three studied species. The numerical values showed that the presence of the solvent molecules has a negligible effect on the energy gap between the HS and LS states, and in all three complexes, this value is nearly equal to 0.5 eV. As the experimental results suggest that the interplay between both the spin magnetism and the orbital magnetism of the studied complexes is most likely the reason for the observed magnetic behavior, as well as for the *g*-tensor anisotropies confirmed by the ESR spectra, we analyzed the delocalization of molecular orbitals and the spin density. Fig. S12 shows the comparison between the extent of the frontier orbitals in the presence of different solvents for the quartet states with $S = 3/2$. The frontier orbitals are mostly ligand in character in all three cases. The delocalization of the highest singly occupied molecular orbital, denoted as the HOMO, and the lowest unoccupied molecular orbital, denoted as the LUMO, is nearly the same in all three studied complexes. In the case of ethylene glycol as a solvent, one can notice that the portion of the HOMO that can be found in the solvent is bigger than in the other two complexes.

To gain a deeper insight into the solvent effects, we repeated our DFT calculations at the same level of theory for the unit cells without the solvent molecules, paying particular attention to the charge and spin density distribution. Analyzing the spin density distribution, we conclude that there are no significant differences between the species with and without the solvent molecule (Fig. S13). The calculated Mulliken atomic spin densities of the Co atom are 2.690 for

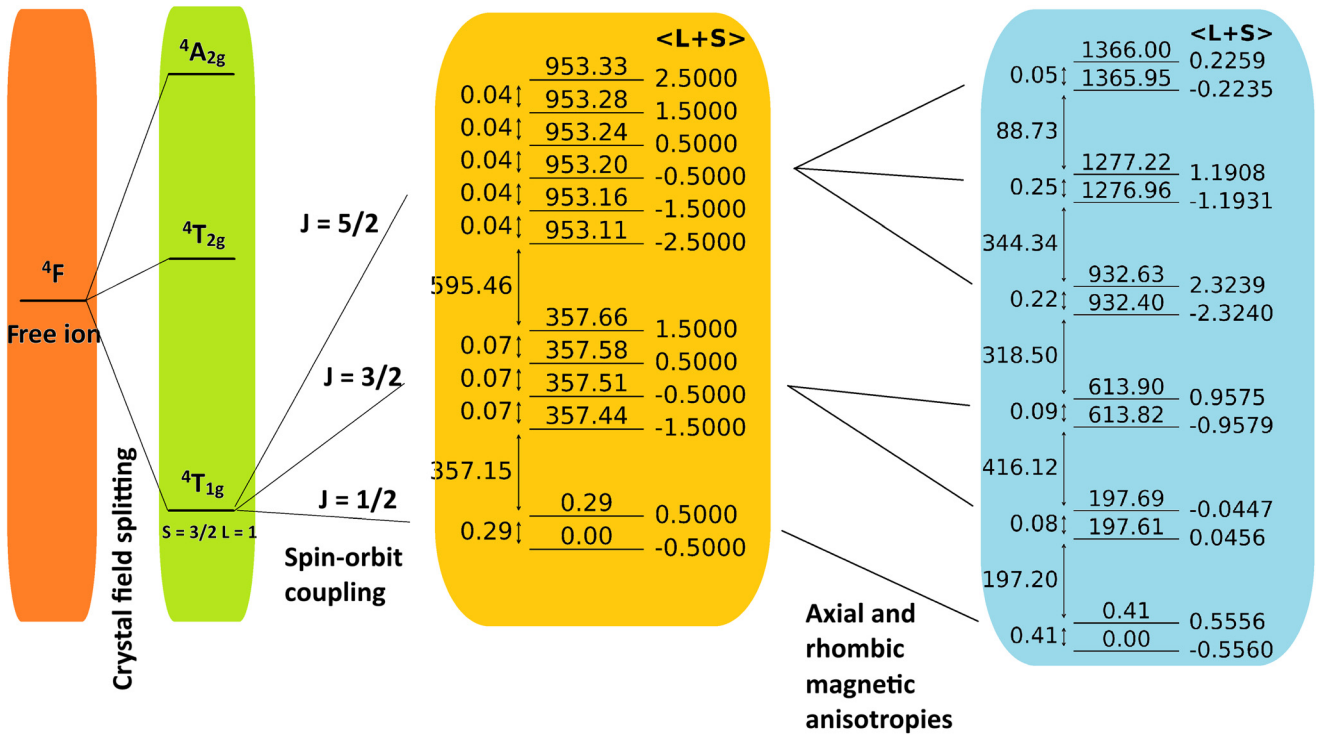

Fig. 11 Energy diagram showing splitting of the free ion ^4F term in the octahedral crystal field by spin–orbit coupling and magnetic anisotropies of the **1**·MeOH complex calculated for fit parameters under a magnetic field of 1000 Oe parallel to the *z* magnetic axis. Energies in cm^{-1} are written on solid lines that represent energy levels. On the left and right sides of the energy levels, the energy gap and the corresponding total spin $J = L + S$ for each energy level are given, respectively.

1·MeOH and 2.694 without the methanol molecule; 2.688 for **1**·EtOH and 2.693 without the ethanol molecule; 2.692 for **1**·EtGly and 2.694 without the ethylene glycol molecule, respectively. Partial electrical charges on the Co atom are 0.464 for **1**·MeOH with and without the methanol molecule; 0.464 for **1**·EtOH and 0.463 without the ethanol molecule; 0.466 for **1**·EtGly and 0.461 without the ethylene glycol molecule, respectively. Fig. S14, S15 and S16 show the comparison of the partial atomic charges on the ligands for the three studied complexes with and without the solvent molecules for **1**·MeOH, **1**·EtOH and **1**·EtGly, respectively. The most pronounced differences are observed in the chloranilate ligand. If we compare the relative changes of the partial charges, we can conclude that in the case of ethylene glycol as a solvent, these changes are somewhat higher than in the other two cases. DFT calculations in the absence of the solvent molecules were performed by using the geometry of the crystal structures grown in the presence of the solvent molecule, which explains the slight differences in the partial charges of the unit cells without the solvent molecules.

The obtained results for the spin density distribution shown in Fig. S13 support the ESR measurements, which are in favor of weak intermolecular spin–spin interactions. Hence, the observed effects of the solvent molecules on the spin density distribution practically exclude the possibility for solvent-mediated long-range interaction in the studied complexes. The observed differences in the magnetic properties are rather attributed to solvent effects on the packing, which lead for example to shorter Co–Co distances in the complex involving MeOH. On the other hand, the local changes of the partial atomic charges in the presence of the solvent molecules influence the magnetic properties of the complexes by altering the electron distribution and inducing changes in the electronic environment of the cobalt ion. This would also affect the molecular orbital delocalization, as well as the spin–orbit coupling. Relating the results obtained from DFT calculations with the experimentally studied magnetic properties, one can conclude that the interplay between the packing of molecules in the crystal and the subtle local effects of solvents on the molecular electronic properties dictates the magnetic response of the studied complexes by influencing the effective magnetic moments and their ordering.

However, it should be emphasized that in this work, we performed only some preliminary basic DFT calculations along with extensive experimental investigations and a detailed model Hamiltonian study. To fully comprehend the underlying reasons for the observed effects on the magnetic properties, additional DFT and *ab initio* calculations, employing the complete active space self-consistent field (CASSCF) method, should be conducted in future work.[17,52–59]

3. Conclusions

Here, we aim to highlight the influence of the exchange of only solvent molecules on the magnetic properties of mononuclear transition-metal complexes. Using the mononuclear cobalt(II) family as an example, it has been demonstrated that, at first sight seemingly irrelevant, the exchange of solvent molecules can notably influence the magnetic properties of structurally very similar complexes. The comprehensive magneto-structural analysis presented here suggests an important role of small variation beyond the first coordination spheres. Namely, hydrogen bonding and aromatic stacking determine the arrangement of molecules in the crystal. Therefore, only solvent exchange, through its influence on crystal packing, can produce subtle magnetic differences, such as variations in *g*-factor values, ZFS parameters, and magnetization relaxation processes.

Conflicts of interest

There are no conflicts to declare.

Data availability

The data supporting this article are given in the supplementary information (SI). The other findings of this study are available from the corresponding authors upon request. Supplementary information: experimental (chapter S1), crystallographic details (Tables S1–S4 and Fig. S1–S7), magnetic susceptibility graph (Fig. S8), magnetic modeling details (Fig. S9 and S10), AC magnetic susceptibility graph (Fig. S11), and DFT visualizations (Fig. S12–S16). See DOI: https://doi.org/10.1039/d5dt02533h.

CCDC 2493719–2493724 contain the supplementary crystallographic data for this paper.[60a–f]

Acknowledgements

This work was supported by the Croatian Science Foundation under the project number [HrZZ-IP-2022-10-9292]. M. H. and N. N. acknowledge support from the project *Cryogenic Centre at the Institute of Physics - KaCIF* (Grant KK.01.1.1.02.0012), co-financed by the Croatian Government and the European Union through the European Regional Development Fund–Competitiveness and Cohesion Operational Programme and the project *Ground states in competition–strong correlations, frustration and disorder - FrustKor* financed by the Croatian Government and the European Union through the National Recovery and Resilience Plan 2021–2026 (NRRP).

References

1 K. Molčanov, B. Kojić-Prodić and A. Meden, Unique Electronic and Structural Properties of 1,4-Benzoquinones: Crystallochemistry of Alkali Chloranilate Hydrates, *Croat. Chem. Acta*, 2009, **82**, 387–396.

2 V. Vuković, K. Molčanov, C. Jelsch, E. Wenger, A. Krawczuk, M. Jurić, L. Androš Dubraja and B. Kojić-Prodić, Malleable Electronic Structure of Chloranilic Acid and Its Species Determined by X-ray Charge Density Studies, *Cryst. Growth Des.*, 2019, **19**, 2802–2810.
3 S. Kitagawa and S. Kawata, Coordination compounds of 1,4-dihydroxybenzoquinone and its homologues. Structures and properties, *Coord. Chem. Rev.*, 2002, **224**, 11–34.
4 S. Kitagawa and R. Matsuda, Chemistry of coordination space of porous coordination polymers, *Coord. Chem. Rev.*, 2007, **251**, 2490–2509.
5 M. Kabir, N. Miyazaki, S. Kawata, K. Adachi, H. Kumagai, K. Inoue, S. Kitagawa, K. Iijima and M. Katada, Novel layered structures constructed from iron–chloranilate compounds, *Coord. Chem. Rev.*, 2000, **198**, 157–169.
6 M. L. Mercuri, F. Congiu, G. Concas and S. A. Sahadevan, Recent Advances on Anilato-Based Molecular Materials with Magnetic and/or Conducting Properties, *Magnetochemistry*, 2017, **3**, 17.
7 M. Atzori, S. Benmansour, G. Mínguez Espallargas, M. Clemente-León, A. Abhervé, P. Gómez-Claramunt, E. Coronado, F. Artizzu, E. Sessini, P. Deplano, A. Serpe, M. L. Mercuri and C. J. Gómez García, A Family of Layered Chiral Porous Magnets Exhibiting Tunable Ordering Temperatures, *Inorg. Chem.*, 2013, **52**, 10031–10040.
8 M. Atzori, F. Pop, P. Auban-Senzier, C. J. Gómez-García, E. Canadell, F. Artizzu, A. Serpe, P. Deplano, N. Avarvari and M. L. Mercuri, Structural Diversity and Physical Properties of Paramagnetic Molecular Conductors Based on Bis(ethylenedithio)tetrathiafulvalene (BEDT-TTF) and the Tris(chloranilato)ferrate(III) Complex, *Inorg. Chem.*, 2014, **53**, 7028–7039.
9 M. Atzori, F. Pop, P. Auban-Senzier, R. Clérac, E. Canadell, M. L. Mercuri and N. Avarvari, Complete Series of Chiral Paramagnetic Molecular Conductors Based on Tetramethylbis(ethylenedithio)-tetrathiafulvalene (TM-BEDT-TTF) and Chloranilate-Bridged Heterobimetallic Honeycomb Layers, *Inorg. Chem.*, 2015, **54**, 3643–3653.
10 B. F. Abrahams, M. J. Grannas, T. A. Hudson, S. A. Hughes, N. H. Pranoto and R. Robson, Synthesis, structure and host-guest properties of $(Et_4N)_2$ $[Sn^{iv}Ca^{ii}$ (chloranilate)$_4]$, a new type of robust microporous coordination polymer with a 2D square grid structure, *Dalton Trans.*, 2011, **40**, 12242–12247.
11 S. Benmansour, C. Vallés-García, P. Gómez-Claramunt, G. Mínguez Espallargas and C. J. Gómez-García, 2D and 3D Anilato-Based Heterometallic M(I)M(III) Lattices: The Missing Link, *Inorg. Chem.*, 2015, **54**, 5410–5418.
12 D. Kowalkowska-Zedler, A. Dołęga, N. Nedelko, R. Łyszczek, P. Aleshkevych, I. Demchenko, J. Łuczak, A. Ślawska-Waniewska and A. Pladzyk, Structural, magnetic and spectral properties of tetrahedral cobalt(II) silanethiolates: a variety of structures and manifestation of field-induced slow magnetic relaxation, *Dalton Trans.*, 2020, **49**, 697–710.
13 K. Uemura, S. Kitagawa, M. Kondo, K. Fukui, R. Kitaura, H.-C. Chang and T. Mizutani, Novel Flexible Frameworks of Porous Cobalt(II) Coordination Polymers That Show Selective Guest Adsorption Based on the Switching of Hydrogen-Bond Pairs of Amide Groups, *Chem. – Eur. J.*, 2002, **8**, 3586–3600.
14 A. Abragam and B. Bleaney, *Electron Paramagnetic Resonance of Transition Ions*, Clarendon Press, Oxford, UK, 1970.
15 J. H. V. Vleck, The Dipolar Broadening of Magnetic Resonance Lines in Crystals, *Phys. Rev.*, 1948, **74**, 1168–1183.
16 S. Ghosh, S. Kamilya, S. Mehta, R. Herchel, M. Kiskin, S. Veber, M. Fedin and A. Mondal, Effect of Ligand Chain Length for Tuning of Molecular Dimensionality and Magnetic Relaxation in Redox Active Cobalt(II) EDOT Complexes (EDOT=3,4-Ethylenedioxythiophene), *Chem. – Asian J.*, 2022, **17**, e202200404.
17 S. Gómez-Coca, A. Urtizberea, E. Cremades, P. J. Alonso, A. Camón, E. Ruiz and F. Luis, Origin of slow magnetic relaxation in Kramers ions with non-uniaxial anisotropy, *Nat. Commun.*, 2014, **5**, 4300.
18 S. Paul, M. Dolai, J. N. Goswami, B. Bhattacharya, F. Emmerling, M. G. B. Drew, S. Chattopadhyay, R. S. Sarkar, A. Sunil, G. Novitchi, E. Moreno-Pineda and W. Wernsdorfer, From strong to weak interaction: reconciling SQUID and μSQUID-EPR data in anomalous Co(ii) dimers, *Inorg. Chem. Front.*, 2025, **12**, 6460–6472.
19 M. Mesić, M. Dunatov, A. Puškarić, G. Medak, R. Kruk and L. Androš Dubraja, Engineering solid-state structural transformations and reactions in complexes containing a natural alkaloid for specific switchable properties, *Inorg. Chem. Front.*, 2025, **12**, 7863–7873.
20 M. Atzori, A. Serpe, P. Deplano, J. A. Schlueter and M. L. Mercuri, Tailoring magnetic properties of molecular materials through non-covalent interactions, *Inorg. Chem. Front.*, 2015, **2**, 108–115.
21 K. Molčanov, M. Jurić and B. Kojić-Prodić, Stacking of metal chelating rings with π-systems in mononuclear complexes of copper(II) with 3,6-dichloro-2,5-dihydroxy-1,4-benzoquinone (chloranilic acid) and 2,2′-bipyridine ligands, *Dalton Trans.*, 2013, **42**, 15756–15765.
22 K. Molčanov, M. Jurić and B. Kojić-Prodić, A novel type of coordination mode of chloranilic acid leading to the formation of polymeric coordination ribbon in the series of mixed-ligand copper(II) complexes with 1,10-phenanthroline, *Dalton Trans.*, 2014, **43**, 7208–7218.
23 L. Androš Dubraja, K. Molčanov, D. Žilić, B. Kojić-Prodić and E. Wenger, Multifunctionality and size of the chloranilate ligand define the topology of transition metal coordination polymers, *New J. Chem.*, 2017, **41**, 6785–6794.
24 M. Pinsky and D. Avnir, Continuous Symmetry Measures. 5. The Classical Polyhedra, *Inorg. Chem.*, 1998, **37**, 5575–5582.
25 R. Ketkaew, Y. Tantirungrotechai, P. Harding, G. Chastanet, P. Guionneau, M. Marchivie and D. J. Harding, OctaDist: a tool for calculating distortion parameters in spin crossover and coordination complexes, *Dalton Trans.*, 2021, **50**, 1086–1096.

26 O. Kataeva, K. Metlushka, K. Ivshin, Z. Yamaleeva, R. Zinnatullin, K. Nikitina, E. Badeeva, V. Khrizanforova, Y. Budnikova, M. Naumann, C. Wellm, A. Alfonsov, V. Kataev, B. Büchner and M. Knupfer, Supramolecular chirality in the crystals of mononuclear and polymeric cobalt(II) complexes with enantiopure and racemic N-thiophosphorylated thioureas, *CrystEngComm*, 2021, **23**, 2081–2090.

27 S. Stoll and A. Schweiger, EasySpin, a comprehensive software package for spectral simulation and analysis in EPR, *J. Magn. Reson.*, 2006, **178**, 42–55.

28 O. Kahn, *Molecular Magnetism*, Wiley-VCH Inc., 1993.

29 A. Carrington and A. D. McLachlan, *Introduction to Magnetic Resonance*, Harper and Row, New York, 1967.

30 D. Žilić, K. Molčanov, M. Jurić, J. Habjanič, B. Rakvin, Y. Krupskaya, V. Kataev, S. Wurmehl and B. Büchner, 3D oxalate-based coordination polymers: Relationship between structure, magnetism and color, studied by high-field ESR spectroscopy, *Polyhedron*, 2017, **126**, 120–126.

31 C. Wellm, W. Roscher, J. Zeisner, A. Alfonsov, R. Zhong, R. J. Cava, A. Savoyant, R. Hayn, J. van den Brink, B. Büchner, O. Janson and V. Kataev, Frustration enhanced by Kitaev exchange in a $\tilde{j}_{\mathrm{eff}}$=1/2 triangular antiferromagnet, *Phys. Rev. B:Condens. Matter Mater. Phys.*, 2021, **104**, L100420.

32 S. Stoll, *EasySpin–EPR spectrum simulation*, https://www.easyspin.org.

33 A. A. Pavlov, J. Nehrkorn, S. V. Zubkevich, M. V. Fedin, K. Holldack, A. Schnegg and V. V. Novikov, A Synergy and Struggle of EPR, Magnetometry and NMR: A Case Study of Magnetic Interaction Parameters in a Six-Coordinate Cobalt (II) Complex, *Inorg. Chem.*, 2020, **59**, 10746–10755.

34 S. A. Cockle, S. Lindskog and E. Grell, Electron-paramagnetic-resonance studies on cobalt(II) carbonic anhydrase–sulphonamide complexes, *Biochem. J.*, 1974, **143**, 703–715.

35 H. R. Jiménez, J. Salgado, J. M. Moratal and I. Morgenstern-Badarau, EPR and Magnetic Susceptibility Studies of Cobalt(II)- and Nickel(II)-Substituted Azurins from Pseudomonas aeruginosa. Electronic Structure of the Active Sites, *Inorg. Chem.*, 1996, **35**, 2737–2741.

36 M. Goldman, *Spin Temperature and NMR in Solids*, Oxford University Press, UK, 1970.

37 L. Androš, M. Jurić, P. Planinić, D. Žilić, B. Rakvin and K. Molčanov, New mononuclear oxalate complexes of copper(II) with 2D and 3D architectures: Synthesis, crystal structures and spectroscopic characterization, *Polyhedron*, 2010, **29**, 1291–1298.

38 C. P. Poole Jr., *Electron Spin Resonance: A Comprehensive Treatise on Experimental Techniques*, John Wiley and Sons, Inc., New York, 1983.

39 J. E. Wertz and J. R. Bolton, *Electron Spin Resonances, Elementary Theory and Practical Applications*, McGraw-Hill, New York, 1972.

40 S. Mugiraneza and A. M. Hallas, Tutorial: a beginner's guide to interpreting magnetic susceptibility data with the Curie-Weiss law, *Commun. Phys.*, 2022, **5**, 95.

41 Y. Wang, R. Li, Q. Wang, L. Yu, G. Yang and D. Liao, Synthesis, structure and properties of two bimetallic compounds $[Co(bpy)_2\ (NiL)]\ (ClO_4)_2$ and $[Co(phen)_3](NiL)\ (ClO_4)_2$ containing a macrocyclic oxamide ligand, *Transition Met. Chem.*, 2004, **29**, 728–731.

42 A. Caneschi, A. Dei, D. Gatteschi and V. Tangoulis, Antiferromagnetic Coupling in a Six-Coordinate High Spin Cobalt(II)-Semiquinonato Complex, *Inorg. Chem.*, 2002, **41**, 3508–3512.

43 M. Pacheco, A. Cuevas, J. González-Platas, F. Lloret, M. Julve and C. Kremer, The crystal structure and magnetic properties of 3-pyridinecarboxylate-bridged Re(ii)M(ii) complexes (M = Cu, Ni, Co and Mn), *Dalton Trans.*, 2015, **44**, 11636–11648.

44 M. Chegerev, D. Korchagin, G. Shilova, N. Efimov, A. Starikov, A. Piskunov, A. Chernyshev, A. Bulgakov, V. Minkin, A. Palii and S. Aldoshin, Magnetically bistable cobalt-dioxolene complexes with a tetradentate N-donor base, *Dalton Trans.*, 2022, **51**, 16876–16889.

45 J. Vallejo, M. Viciano-Chumillas, F. Lloret, M. Julve, I. Castro, J. Krzystek, M. Ozerov, D. Armentano, G. D. Munno and J. Cano, Coligand Effects on the Field-Induced Double Slow Magnetic Relaxation in Six-Coordinate Cobalt(II) Single-Ion Magnets (SIMs) with Positive Magnetic Anisotropy, *Inorg. Chem.*, 2019, **58**, 15726–15740.

46 I. Gryca, J. Palion-Gazda, B. Machura, M. Penkala, F. Lloret and M. Julve, Heterobimetallic Oxalate-Bridged MIIReIV (M = Zn, Cu, Ni, Co and Mn) Complexes Incorporating Bis(3,5-dimethylpyrazol-1-yl)methane: Synthesis and Magneto-Structural Studies, *Eur. J. Inorg. Chem.*, 2016, **2016**, 5418–5426.

47 M. Mocanu, A. Patrascu, M. Hillebrand, S. Shova, F. Lloret, M. Julve and M. Andruh, Trinuclear Nickel(II) and Cobalt(II) Complexes Constructed from Mannich–Schiff-Base Ligands: Synthesis, Crystal Structures, and Magnetic Properties, *Eur. J. Inorg. Chem.*, 2019, **2019**, 4773–4783.

48 L. Vahovska, S. Vitushkina, I. Potočňak, Z. Travniček and R. Herchel, Effect of linear and non-linear pseudohalides on the structural and magnetic properties of Co(ii) hexacoordinate single-molecule magnets, *Dalton Trans.*, 2018, **47**, 1498–1512.

49 W. C. Pereira, C. Pinheiro, F. Lloret and M. Julve, Towards oxalate-bridged iron(II), cobalt(II), nickel(II) and zinc(II) complexes through oxotris(oxalato)niobate(v): an open air non-oxidizing synthetic route, *Inorg. Chem. Front.*, 2018, **5**, 1294–1306.

50 V. Tangoulis, M. Lalia-Kantouri, M. Gdaniec, C. Papadopoulos, V. Miletic and A. Czapik, New Type of Single Chain Magnet: Pseudo-One-Dimensional Chain of High-Spin Co(II) Exhibiting Ferromagnetic Intrachain Interactions, *Inorg. Chem.*, 2013, **52**, 6559–6569.

51 S. Kundu, S. Roy, K. Bhar, R. Ghosh, C. Lin, J. Ribas and B. Ghosh, Synthesis, molecular and crystalline architectures, and properties of a mononuclear complex $[Co^{II}(benzidine)_2\ (NCS)_2\ (OH_2)_2]$, *J. Chem. Sci.*, 2013, **125**, 723–730.

52 G. K. Gransbury, M.-E. Boulon, R. A. Mole, R. W. Gable, B. Moubaraki, K. S. Murray, L. Sorace, A. Soncini and C. Boskovic, Single-ion anisotropy and exchange coupling in cobalt(II)-radical complexes: insights from magnetic and ab initio studies, *Chem. Sci.*, 2019, **10**, 8855–8871.

53 C. C. D. Centre, *ConQuest*, https://www.ccdc.cam.ac.uk/solutions/software/conquest/.

54 T. Jurca, A. Farghal, P.-H. Lin, I. Korobkov, M. Murugesu and D. S. Richeson, Single-Molecule Magnet Behavior with a Single Metal Center Enhanced through Peripheral Ligand Modifications, *J. Am. Chem. Soc.*, 2011, **133**, 15814–15817.

55 J. M. Zadrozny and J. R. Long, Slow Magnetic Relaxation at Zero Field in the Tetrahedral Complex $[Co(SPh)_4]^{2-}$, *J. Am. Chem. Soc.*, 2011, **133**, 20732–20734.

56 C. V. Topping and S. J. Blundell, A.C. susceptibility as a probe of low-frequency magnetic dynamics, *J. Phys.: Condens. Matter*, 2018, **31**, 013001.

57 A. D. Becke, Density-functional exchange-energy approximation with correct asymptotic behavior, *Phys. Rev. A*, 1988, **38**, 3098.

58 C. Lee, W. Yang and R. G. Parr, Development of the Colle-Salvetti correlation-energy formula into a functional of the electron density, *Phys. Rev. B:Condens. Matter Mater. Phys.*, 1988, **37**, 785.

59 M. Iakovleva, T. Petersen, A. Alfonsov, Y. Skourski, H.-J. Grafe, E. Vavilova, R. Nath, L. Hozoi and V. Kataev, Static magnetic and ESR spectroscopic properties of the dimer-chain antiferromagnet BiCoPO 5, *Phys. Rev. Mater.*, 2022, **6**, 094413.

60 (*a*) CCDC 2493719: Experimental Crystal Structure Determination, 2026, DOI: 10.5517/ccdc.csd.cc2ppxkw; (*b*) CCDC 2493720: Experimental Crystal Structure Determination, 2026, DOI: 10.5517/ccdc.csd.cc2ppxlx; (*c*) CCDC 2493721: Experimental Crystal Structure Determination, 2026, DOI: 10.5517/ccdc.csd.cc2ppxmy; (*d*) CCDC 2493722: Experimental Crystal Structure Determination, 2026, DOI: 10.5517/ccdc.csd.cc2ppxnz; (*e*) CCDC 2493723: Experimental Crystal Structure Determination, 2026, DOI: 10.5517/ccdc.csd.cc2ppxp0; (*f*) CCDC 2493724: Experimental Crystal Structure Determination, 2026, DOI: 10.5517/ccdc.csd.cc2ppxq1.